EES Solar

ROYAL SOCIETY OF CHEMISTRY

PAPER

View Article Online
View Journal | View Issue

Check for updates

Cite this: *EES Sol.*, 2025, **1**, 310

Tuning $FAPbI_3$ for scalable perovskite indoor photovoltaics†

Victor Marrugat-Arnal,[a] Wanlong Wang,[a] Mohammad Reza Kokaba,[a] Sergey Dayneko,[b] Dongyang Zhang,[b] Shuang Qiu,[b] Vishal Yeddu,[b] Yameen Ahmed,[a] Augusto Amaro,[b] Muhammad Awais[a] and Makhsud I. Saidaminov*[ab]

Received 26th November 2024
Accepted 11th April 2025

DOI: 10.1039/d4el00030g

rsc.li/EESSolar

We report cesium lead bromide ($CsPbBr_3$)-alloyed formamidinium lead iodide ($FAPbI_3$) perovskites for scalable fabrication of indoor photovoltaics. We find that simultaneous alloying of $FAPbI_3$ with Cs and Br *via* $CsPbBr_3$ single crystals prolongs charge carrier lifetimes beyond 1 μs, and improves the morphology of perovskite films fabricated by blade coating in ambient air. The resulting alloy exhibits an improved bandgap alignment with the IEC TS 62607 B4 standard light spectrum, corresponding to white LED illumination, which leads to improved photovoltage. As a result, we report indoor solar cells with a power conversion efficiency of 32.6% for 0.049 cm^2 active-area devices; and 28.1% for 10.23 cm^2 modules under white LED illumination. Halide segregation, surprisingly, shows limited impact on the stability of these solar cells, which maintain 80% of their initial performance following 500 hours of operation under continuous high-irradiance indoor light.

Broader context

Indoor photovoltaics are rapidly emerging for powering several increasingly ubiquitous technologies demanding efficient, low-cost, and sustainable energy solutions. Already making significant inroads into industrial processes, Internet of Things (IoT) is the most prominent example. Achieving high power conversion efficiency under indoor lighting is critical to meeting sustainable energy needs, yet current photovoltaic technologies, such as silicon, fall short due to their suboptimal bandgap for low-light conditions. Perovskites, with their tunable bandgap, offer a compelling alternative. However, most studies to date have focused on laboratory-scale fabrication methods, leaving a gap in understanding how to scale these materials for practical, industrial applications. In this work, we address this challenge by demonstrating scalable fabrication methods for perovskite solar cells (PSCs) specifically designed for indoor applications. Leveraging bandgap tunability and enhanced morphological and photophysical properties, our industrially scalable devices achieved efficiencies exceeding the theoretical limit for silicon solar cells under LED illumination. Our approach not only advances the scientific understanding of scalable indoor photovoltaics but also sets the stage for perovskites to play a pivotal role in powering the future of indoor energy harvesting.

Introduction

Halide perovskites have been extensively studied for photovoltaic applications in the last decade. Harnessing their optical and electronic properties[1] resulted in a steep improvement in the power conversion efficiency (PCE) of perovskite solar cells (PSCs), although this progress has now started to plateau.[2] Under 1.5 air mass (AM 1.5) illumination, also known as 1 sun, the theoretical maximum PCE for a single-junction solar cell is 33.3%.[3] Considering intrinsic properties of an absorber material, studies show that the maximum attainable PCEs are 28.3 ÷ 29.43% for silicon,[4,5] and 27 ÷ 29.53% for PSCs.[6,7] Experimentally, silicon and PSCs have reached record PCEs of 27.3% and 27.0%,[2,8] respectively, close to their theoretical limits. This indicates experimental saturation and effective interchangeability between silicon and perovskite absorbers under 1 sun illumination.

The solar cell performance landscape changes under other types of illumination. For instance, indoor lighting's narrow emission spectrum allows for increasing the absorber's bandgap and thus the device's open-circuit voltage (V_{OC}) without sacrificing the absorption of part of the light, as would occur under 1 sun spectrum. Theoretical calculations suggest that wide-bandgap absorbers (~1.9 eV) can achieve PCEs above 50% under white LED illumination, which is ~20% higher than the one achievable by any single-junction solar cell under 1 sun.[9,10] Therefore, with a bandgap of 1.12 eV,[9] silicon is not an optimal material for harvesting indoor light; in contrast, the tunable bandgap of perovskites makes them ideally suited for this application.[11–13]

---

[a] Department of Electrical & Computer Engineering, University of Victoria, 3800 Finnerty Road, Victoria, BC V8P 5C2, Canada. E-mail: msaidaminov@uvic.ca

[b] Department of Chemistry, University of Victoria, 3800 Finnerty Road, Victoria, BC V8P 5C2, Canada. E-mail: msaidaminov@uvic.ca

† Electronic supplementary information (ESI) available. See DOI: https://doi.org/10.1039/d4el00030g

Perovskites have therefore become a focal point for indoor photovoltaics.[14–26] Unlike the standardized equipment and protocols established for 1 sun photovoltaics, indoor photovoltaics lack a widely-adopted reference framework, complicating the measurements and comparison of efficiencies.[27] For accurate and consistent indoor PSC PCE measurements, either a reference cell specifically designed for white LED spectrum is needed,[25,27] or the input irradiance should be characterized.[14–23,26,28,29] The equipment used for the last method (usually, a calibrated spectroradiometer) varies across laboratories.

Additionally, the uncertainty in the input power (P_{IN}) is frequently overlooked. Combined with potential errors in output power (P_{OUT}) measurements, these uncertainties can significantly impact the claimed PCEs for indoor photovoltaics. Moreover, the differences in the spectra of the LED sources used across different laboratories impact on the reproducibility and understanding of photovoltaic performance in indoor settings. Thus, P_{IN} matching can enable laboratory-to-laboratory comparisons if only it is paired with light source spectral matching, especially for evaluating specific figures of merit like solar cell's short-circuit current density (J_{SC}). It is also important to note that, because part of the white LED spectrum lies outside the visible range,[28] estimating P_{IN} using an illuminance-to-irradiance conversion is inaccurate. To address these discrepancies and facilitate laboratory-to-laboratory comparability of indoor PSCs following procedures similar to those of solar photovoltaics, here we will use a reference photovoltaic cell calibrated in the National Institute of Standards and Technology (NIST)[30] to match our indoor light source to a standardized one.

Previous experimental works have reported over 40% PCE under 1000 lux white LED light.[17–20,22,26] For instance, Wang *et al.* achieved a 41.2% PCE using a 1.69 eV cesium lead iodide ($CsPbI_3$) PSC.[22] Unfortunately, this perovskite composition faces structural stability issues due to its low Goldschmidt tolerance factor.[31] By partially substituting Cs by formamidinium (FA), and methylammonium (MA), Liu *et al.* achieved a PCE of 41.33% with a 1.52 eV flexible PSC. The reduced bandgap resulted in a V_{OC} under 1 V, which was compensated by an uncommon 84.32% fill factor (FF).[19] However, as previously discussed, increasing the bandgap of iodine-based perovskites is desirable, given the potential to exceed 50% efficiency. The inclusion of bromine is an effective method to widen the bandgap,[11,24] as demonstrated by Li *et al.*, who achieved a 1.79 eV bandgap and V_{OC} surpassing 1.1 V, resulting in a 41.58% PCE.[17] More recently, Shi *et al.* used the same family of perovskites ($FA_{1-x}Cs_xPb(I_{1-y}Br_y)_3$), surpassing 42% PCE with a lower bandgap (1.65 eV),[26] indicating that there is still room for improving PCE in the <1.8 eV range. While halide mixing enables closer approaches to the optimal bandgap for harvesting white LED light, it introduces a major degradation source through the halide segregation phenomenon.[12,13,32–34] To mitigate this phenomenon, ammonium salts,[17] or chlorine,[35] have been incorporated in the perovskite film. However, the performance of low-bromine containing perovskites in PSCs under indoor light remains underexplored. Moreover, a spectral analysis of the light sources, showing the maximum J_{SC} attainable by integrating the PSC's external quantum efficiency (EQE) with the light source's spectral data, is often lacking in these studies. It is also worth mentioning that among the studies reviewed, only one reports scalable fabrication of indoor PSCs based on methylammonium lead iodide ($MAPbI_3$),[16] a perovskite that is currently largely abandoned due to its instability.[36,37]

Here we study the combined effect of bromine and cesium on the bandgap of one of the most stable perovskites, $FAPbI_3$, while preserving its intrinsic properties. This approach is informed by literature reporting high efficiency and stability for $FACsPbI_3$ perovskites,[38] as well as the aforementioned studies demonstrating bandgap widening with bromine addition. By limiting both Cs and Br additives to 9 mol%, we prevent significant crystallographic changes in $FAPbI_3$, and minimize harmful levels of halide segregation, without needing additives that alter the perovskite's final composition. Through alloying $CsPbBr_3$ and $FAPbI_3$, we developed a $Cs_{0.03}FA_{0.97}Pb(Br_{0.1}I_{0.9})_3$ ink, which we deposited *via* blade coating, thus demonstrating scalable fabrication of indoor perovskite photovoltaics.

Results and discussion

Impact of Cs and Br on ambient-air scalable deposition of $FAPbI_3$ films

We recently reported blade-coated n-i-p-structured $FAPbI_3$ PSCs achieving a 22.7% PCE under 1 sun illumination.[39] Our perovskite ink, optimized for scalable deposition in ambient air, employed a 2-methoxyethanol/*N*-methyl-2-pyrrolidone (2ME/NMP) solvent system. Despite its good performance under 1 sun, the $FAPbI_3$ bandgap of ~1.5 eV must be widened to optimize performance for indoor light harvesting. To accomplish this, we chose to incorporate $CsPbBr_3$ single crystals into $FAPbI_3$, for simultaneous Cs and Br mixing.

We first studied the bandgap tunability of perovskite films derived from our $FAPbI_3$ scalable ink. Pre-made $CsPbBr_3$ single crystals were added into the $FAPbI_3$ solution (Fig. 1a), then the mixture was agitated for >3 hours to maximize $CsPbBr_3$ dissolution, followed by filtration to remove undissolved salts. The solution was then deposited onto substrates by blade coating and annealed to form perovskite films. The films exhibited an increasing bandgap with higher $CsPbBr_3$ content, which saturated at 1.58 eV due to limited solubility of $CsPbBr_3$ (Fig. 1b). We selected the saturated composition, $(CsPbBr_3)_{0.09}(FAPbI_3)_{0.91}$ (referred as "CPB/FAPI alloy" in the following) for further study, as it was the widest bandgap within our experimental range. To further inquire into the composition of the filtered CPB/FAPI alloy, we analyzed it under energy-dispersive X-ray spectroscopy (EDX) (Fig. S1†), and found that the Cs/Pb atomic ratio went down from 0.09 in the initial mixture to 0.03 on the film, whereas the Br/Pb ratio increased from 0.27 to 0.30. According to these results, the composition of the CPB/FAPI film is $Cs_{0.03}FA_{0.97}Pb(Br_{0.1}I_{0.9})_3$. The exceeding cesium in solution had likely paired with iodine to form CsI precipitate, which was filtered out.

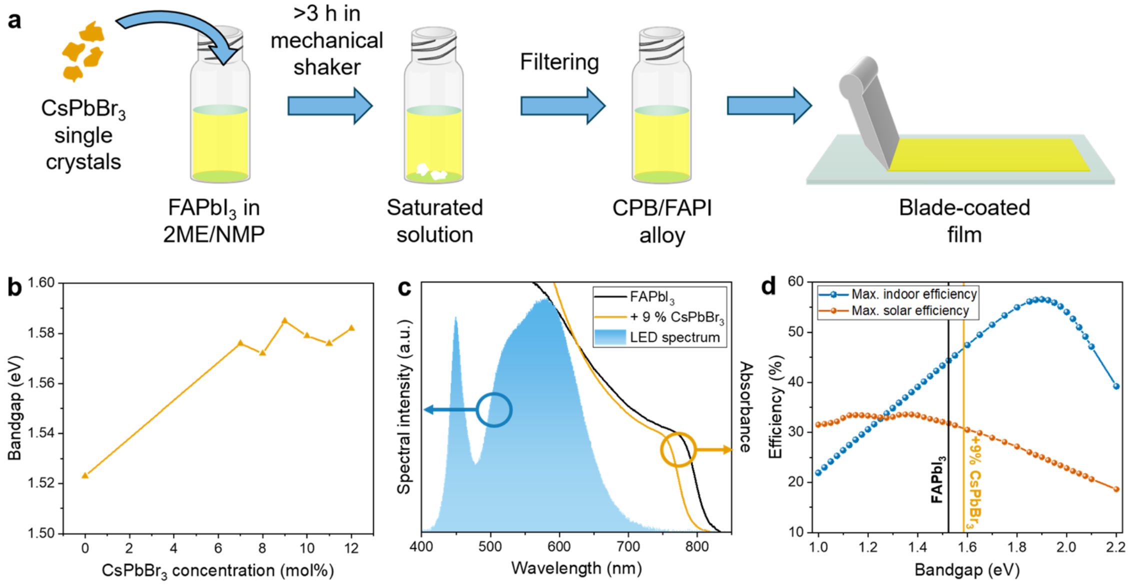

Fig. 1 $FAPbI_3$ bandgap widening *via* $CsPbBr_3$ alloying. (a) Schematic of preparation of perovskite ink and film. (b) Bandgaps extracted from photoluminescence (PL) spectra of $FAPbI_3$-based films prepared with different concentrations of $CsPbBr_3$. (c) Comparison of the spectrum of white LED source and absorbance spectra of the studied perovskite films. (d) Theoretical power conversion efficiency maxima as a function of absorber bandgap for two different light sources: white LED (indoor), and AM 1.5 (solar).

To evaluate the potential of the augmented perovskite film for indoor light harvesting, we measured the spectrum of a white LED source, and compared it with the absorption spectra of $FAPbI_3$ and CPB/FAPI films (Fig. 1c). The absorption spectra of both perovskite films fully covered the LED light spectrum, indicating that both compositions can absorb the white light effectively, so they are expected to yield a similar J_{SC}. At the same time, the theoretical maximum V_{OC} is expected to increase with the bandgap, eventually enhancing the PCE of the CPB/FAPI indoor PSCs.

We quantified the theoretical figures-of-merit of solar cells using a computational code (see ESI† code "max_PCE_calculation.py") considering a black-body model for the calculation of J_{SC}, the Shockley–Queisser model for V_{OC}, and Green's approximation for FF.[9] The resulting theoretical PCEs as a function of bandgap are shown in Fig. 1d for a white LED spectrum with $P_{IN} = 317\ \mu W\ cm^{-2}$ and standard 1 sun illumination. Our results under 1 sun align with previous theoretical calculations showing an optimal bandgap of 1.1–1.4 eV,[3,10,17,40–42] validating our methodology. When the light source is replaced with a white LED spectrum, the optimal bandgap shifts to ~1.9 eV. Our $FAPbI_3$ film has a bandgap of 1.52 eV, while our doping method widens it to 1.58 eV, increasing the theoretical PCE from 44.3% to 46.8%. Although this improvement is modest compared to the theoretical gain from widening the bandgap to 1.9 eV, we chose to investigate its impact on indoor photovoltaic performance. Higher Br content could increase the bandgap further, but risks exacerbating halide segregation; similarly, increasing Cs would necessitate alternative solvent systems, making ambient-air scalable deposition questionable.

Fig. 2a and b show scanning electron microscopy (SEM) images of the control $FAPbI_3$ and CPB/FAPI films deposited *via* blade coating in ambient air conditions at a relative humidity (RH) of ~58%. Under these conditions, the alloying appears to improve film quality by reducing the occurrence of pinholes. Without additives, $FAPbI_3$ requires a low humidity environment to achieve optimum film quality.[43] Small quantities of Cs have been reported to improve the perovskite film's uniformity,[44] and to reduce pinholes[45] under ambient humid conditions. We hypothesize that Cs in $CsPbBr_3$ positively influences the crystallization dynamics during blade coating and annealing, thereby enhancing film morphology. To further investigate this effect, we analyzed Cs-only alloy (+9 mol% CsI) and Br-only alloy (+9 mol% $PbBr_2$) perovskite films. In solution, the Cs-only formulation exhibited similar saturation behavior to the CPB/FAPI alloy, while the Br-only formulation dissolved completely. After filtering the inks, films were fabricated under the same conditions. The Cs-only and CPB/FAPI alloy films showed comparable grain sizes (Fig. 2b and d), suggesting that Cs plays a key role in modifying perovskite crystallization dynamics. In contrast, the Br-doped film consisted of larger grains (Fig. 2c). Although both Cs- and Br-only films showed fewer pinholes, they were still present. Furthermore, they both exhibited larger foreign-phase grains, with the Cs-only film showing a greater abundance. X-ray diffraction (XRD) revealed the presence of PbI_2, with the Cs-only film having the highest PbI_2-to-(001) perovskite peak ratio (Fig. S2†). Unlike the single-element alloys, CPB/FAPI maintained the characteristic $FAPbI_3$ distribution of XRD peak intensities, indicating the cubic perovskite crystal lattice was preserved.[46] Additionally, we prepared +CsI, $PbBr_2$ films from a perovskite ink with the same nominal composition as CPB/FAPI, but using CsI and $PbBr_2$, instead of pre-made $CsPbBr_3$, to make the alloy. Both CPB/FAPI and +CsI, $PbBr_2$ films showed similar perovskite diffraction

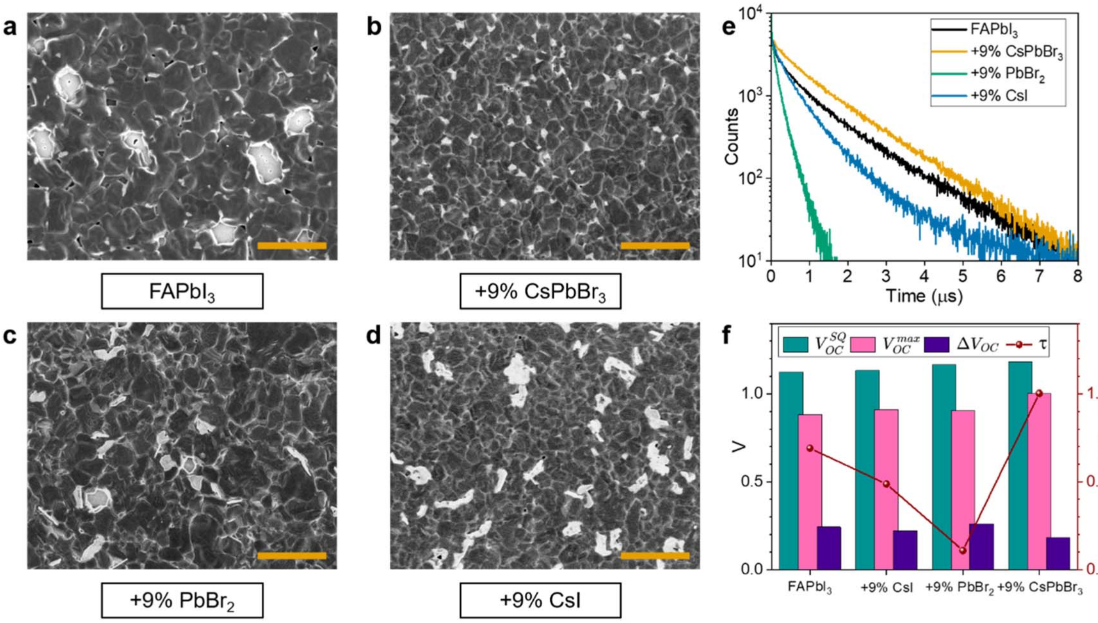

Fig. 2 Morphological and photophysical characterization. SEM images of (a) $FAPbI_3$, (b) CPB/FAPI alloy, (c) Br-only alloy, and (d) Cs-only alloy perovskite films blade coated on indium tin oxide (ITO) and SnO_2. The scale bar represents a length of 5 μm. (e) Time resolved photoluminescence (TRPL) decays of perovskite films deposited on ITO/SnO_2. (f) Comparison of V_{OC} values with charge carrier lifetimes as calculated from TRPL decays, for 58% RH fabrication conditions. V_{OC}^{SQ} is the maximum theoretical limit for V_{OC} considering the bandgap of each composition. V_{OC}^{max} is the maximum V_{OC} obtained from PSCs made from these compositions. ΔV_{OC} is the difference between the last two. τ is the estimated charge carrier lifetime.

patterns, but the +CsI, $PbBr_2$ film showed the presence of unreacted PbI_2 (Fig. S3†). These findings indicate that only the combined doping of Cs and Br *via* pre-made $CsPbBr_3$ crystals is able to maintain the crystallographic properties of $FAPbI_3$, and achieve optimal film morphology and phase-purity.

We proceeded to analyze the photophysical properties of the films by time resolved photoluminescence (TRPL) spectroscopy (Fig. 2e). Among the films, only CPB/FAPI was able to improve the charge carrier lifetime (τ) of $FAPbI_3$, exceeding 1 μs, as measured from the double exponential fitting of the TRPL decay.[47] Fig. 2f compares the measured τ, as well as theoretical calculations and measurements of maximum V_{OC}. For these experimental conditions, we observed an inverse correlation between τ and ΔV_{OC} (the difference between Shockley–Queisser V_{OC} limit and maximum obtained V_{OC}), with Br-only alloying presenting the shortest τ and highest ΔV_{OC}, while CPB/FAPI alloy showed an opposite trend. This suggests a lower concentration of trap states in the CPB/FAPI alloy films. Thus, our findings indicate that, while both Cs and Br separately can enhance film quality under ambient-air conditions, only their combined effect preserves the excellent intrinsic properties of $FAPbI_3$.

Perovskite solar cells for harvesting white LED light

We fabricated PSCs in an n-i-p structure (ITO/SnO_2/KCl/perovskite/*n*-octylammonium iodide (OAI)/Spiro-OMeTAD/gold), and measured their performance under both AM 1.5 solar illumination and white LED light. As noted above, accurate efficiency assessment under a non-standardized light source requires a calibration of the light source. We used a SRI 6014b silicon calibrated reference photovoltaic cell with a filtered glass window from NIST.[30] Fig. S4† shows the calibration setup, which was used to set our white LED source under the International Electrotechnical Commission (IEC) TS 62607-7-2:2023 standard.[48]

We first used a non-standardized white LED for a rapid screening of different compositions of PSCs fabricated under identical conditions. As shown in Fig. S5,† the tendency in efficiency agreed with the theoretical predictions of Fig. 1d and previous reports,[9,49] *i.e.*, V_{OC} increased with the absorber bandgap when switching from 1 sun to LED illumination, while J_{SC} remained the same. The narrow spectrum of the white LED (Fig. 1b) propitiated the similar J_{SC}, as the studied compositions can absorb nearly all incident radiation. But under 1 sun illumination, J_{SC} decreased for the wide-bandgap alloys, again as expected.

We will now compare the performance of PSCs based on $FAPbI_3$ perovskites alloyed with different bandgap-widening additives. CPB/FAPI PSCs showed the highest PCE of 32.6% under white LED illumination (IEC TS 62607-7-2:2023, B4, see Fig. 3a). Cs-only (+9 mol% CsI) alloying reduced the performance of PSCs due to the formation of non-perovskite phases, as discussed above (Fig. S5†). On the other hand, Br-only (+$PbBr_2$ with optimized concentration, Fig. S6†) and +CsI, $PbBr_2$ (Fig. S7†) did show similar performances of champion cells (Fig. 3a–d); however, CPB/FAPI presented a notably higher reproducibility, which correlates with its visually uniform film appearance (Fig. S7 and S8†). In addition, CPB/FAPI PSCs offer

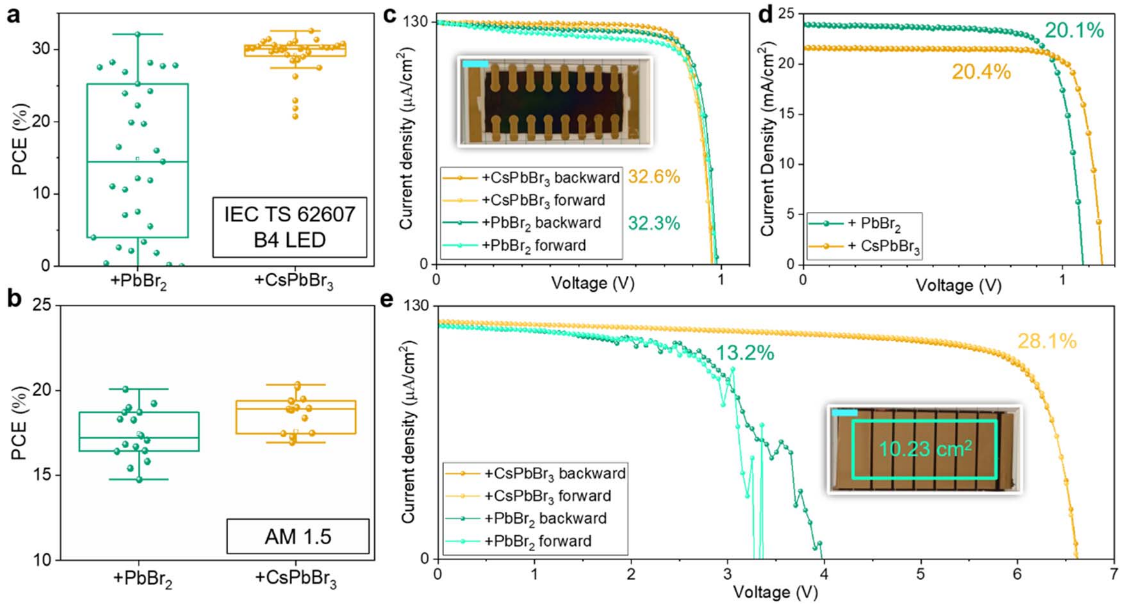

Fig. 3 *JV* performance characterization. (a) Statistical PCE distribution of the backward scans of two 16-pixel devices for different $FAPbI_3$-based alloys under a B4 light source calibrated according to IEC TS 62607-7-2:2023. The boxes indicate the interquartile range (IQR). The whiskers indicate the maximum and minimum data points within 1.5 × IQR. The median and mean are represented by the line dividing the boxes and the open square symbols, respectively. (b) Statistical PCE distribution of the backward scans of 16-pixel devices for different $FAPbI_3$-based alloys under AM 1.5 (1 sun) illumination. (c) *JV* curves of champion 0.049 cm^2 pixels under a calibrated B4 source (inset shows an image of a 16-pixel device, the blue scale bar represents a length of 1 cm), and (d) under AM 1.5 illumination. (e) *JV* curves of champion 10.23 cm^2 modules under a calibrated B4 source (inset shows an image of a 7-cell module, the blue scale bar represents a length of 1 cm, green rectangle indicates the active area of the device).

greater photocurrent stability than Br-only (+$PbBr_2$) alloyed PSCs (Fig. S9†). These findings indicate that although the +$PbBr_2$ and +CsI, $PbBr_2$ alloyings of $FAPbI_3$ show areas with good film quality, they suffer from severe stability and uniformity issues.

To evaluate the scalability of these devices, we fabricated 10.23 cm^2, 7-cell modules by depositing all the layers, except

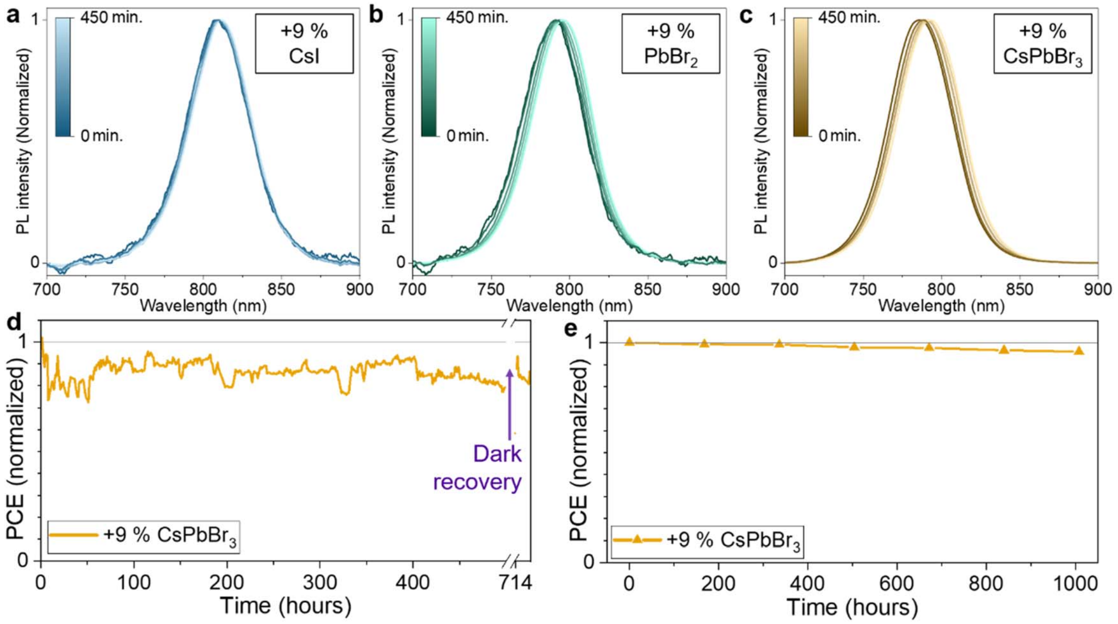

Fig. 4 Stability characterization. PL peak evolution under ~416 μW cm^{-2} white LED illumination of the (a) +9% CsI, (b) +9% $PbBr_2$, (c) +9% $CsPbBr_3$ (CPB/FAPI) films. (d) MPP under 2590 (±3) μW cm^{-2} white LED light, and (e) shelf lifetime stability measurements of a CPB/FAPI alloy PSC.

Table 1 Perovskite inks composition. Weight of precursors needed to form different 0.5 mL of 1 M perovskite inks. Solvents and additives are not included in the table

Composition	PbI_2 (mg)	FAI (mg)	CsI (mg)	$PbBr_2$ (mg)	$CsPbBr_3$ (mg)
$FAPbI_3$	230.5	86.0			
$FA_{0.91}Cs_{0.09}PbI_3$ (+9% CsI)	230.5	78.2	11.7		
$FAPb(Br_{0.05}I_{0.95})_3$ (5% Br)	213.2	86.0		13.8	
$FAPb(Br_{0.10}I_{0.90})_3$ (10% Br)	195.9	86.0		27.5	
$FAPb(Br_{0.15}I_{0.85})_3$ (15% Br)	178.6	86.0		41.3	
$FAPb(Br_{0.20}I_{0.80})_3$ (20% Br)	161.3	86.0		55.1	
$FA_{0.91}Cs_{0.09}Pb(Br_{0.09}I_{0.91})_3$ (+CsI, $PbBr_2$)	199.4	78.2	11.7	24.8	
$FA_{0.91}Cs_{0.09}Pb(Br_{0.09}I_{0.91})_3$ (CPB/FAPI)	209.8	78.2			26.1

gold, on top of P1-prepatterned ITO substrates, scribing P2 with a CO_2 laser, and then depositing gold using P3-patterned masks. Fig. 3e showcases the *JV* curves of the champion modules with the most promising $FAPbI_3$ alloys. Unlike the $PbBr_2$ alloy, the CPB/FAPI module achieved a high PCE of 28.1% under white LED illumination (IEC TS 62607-7-2:2023, B4). The module retains the high fill factor (FF) (76.5%) of the cells, which we attribute to its superior film uniformity. The V_{OC} per cell (module V_{OC}/number of cells) was 0.94 V for CPB/FAPI, close to 0.97 V V_{OC} of the champion pixel for the same composition. We observed a slight reduction in module's J_{SC} which we attribute to small variations in the size of the module's sub-cells, which can be addressed by ultrafast green laser scribing in the future.

Stability of PSCs

$CsPbBr_3$ alloying produced high-quality films with minimal foreign phases, reducing potential stability issues induced by impurities. We hence posit that halide segregation might be the primary challenge to these PSCs. To investigate this, we analyzed the PL peak evolution of alloyed perovskite films under high intensity ($\sim$416 μW cm^{-2}) white LED illumination (Fig. 4a–c), finding indeed instability in +$PbBr_2$ and CPB/FAPI alloy films due to halide de-mixing. However, we also found that this effect is reversible for our composition (Fig. S10†). To evaluate the impact of halide segregation on the PSC lifespan, we tracked the maximum power point (MPP) of an encapsulated PSC with our CPB/FAPI alloy under a higher intensity (2590 ($\pm$3) μW cm^{-2}) white LED illumination in ambient air (Fig. 4d). The device retained 80% of its initial efficiency after 500 hours of continuous operation, indicating the limited effect of halide segregation on our PSCs for indoor light photovoltaics. Assuming that halide segregation is the primary degradation mechanism, we investigated the recovery of the same PSC after >700 hours of continuous operation. To isolate dark recovery effects from other recovery mechanisms, we monitored the evolution of PCE after removing only the electrical bias while keeping the sample illuminated, for which we observed that the tendency was retained. In contrast, upon dark recovery, the device recovered up to 94% of its initial PCE (Fig. 4d). This recovery behavior in PSCs suggests that cyclic dark periods could enhance the long-term stability of these photovoltaic devices by allowing for periodic recovery of efficiency.

To complement the stability study, we periodically measured the performance of another encapsulated CPB/FAPI PSC stored in a low-humidity (<30% RH) ambient environment (Fig. 4e): the device maintained >95% of its initial efficiency after 1000 hours of the shelf-life stability analysis.

Conclusion

Cs and Br alloying *via* $CsPbBr_3$ crystals in $FAPbI_3$ perovskites leads to significant improvements in film morphology and indoor photovoltaic performance. Through a substantial improvement of the film quality, with minimal foreign-phase grains, the optimized $CsPbBr_3$-saturated composition improved the indoor PCE of $FAPbI_3$ by increasing its bandgap, preserving its crystal structure, and enhancing its intrinsic properties. Although halide segregation presents a challenge, its impact on the stability was limited and recoverable, making this composition a promising candidate for stable, scalable indoor photovoltaics. Further investigations on the scalability and stability of perovskites with $\sim$1.9 eV bandgap will be crucial to surpass the 50% efficiency threshold for indoor photovoltaics.

Experimental

Materials

Indium tin oxide (ITO) coated glass substrates were purchased from Shang Yang Solar (X07-10A). Methylammonium chloride (MACl, >99.9%) and formamidinium iodide (FAI, >99.99%) were purchased from Greatcell Solar Materials. Lead iodide (PbI_2, 99.99%) was purchased from Tokyo Chemical Industry. *N*-Octylammonium iodide (OAI) was purchased from Fisher Scientific. Cesium iodide (CsI, 99.9% and 99.999%), lead bromide ($PbBr_2$, 99.999%), cesium bromide (CsBr, 99.9%), dimethyl sulfoxide (DMSO, 99%), tetramethyl ammonium bromide (TMABr), potassium chloride (KCl, 99.999%), 4-*tert*-butylpyridine (*t*BP, 98%), bis(trifluoromethane)sulfonimide lithium (LiTFSI, 99.95%), and cobalt salts (FK 209 Co(III) TFSI), 2-methoxyethanol (2-ME, >99.8%), *N*-methyl-2-pyrrolidone (NMP, $\geq$99%), acetonitrile (ACN, $\geq$99.9%), and chlorobenzene (CB, 99.5%) were purchased from Millipore Sigma. Tin(IV) oxide (SnO_2, 15% in H_2O colloidal dispersion) was purchased from Alfa Aesar. Spiro-OMeTAD was purchased from Xi'an Polymer Light Technology Co., Ltd.

Cesium lead bromide ($CsPbBr_3$) crystal growth

Following previous works,[50,51] CsBr (0.01 mol, 2.13 g), $PbBr_2$ (0.02 mol, 7.34 g) and 12 mL DMSO were added into a vial and stirred at 80 °C for 24 hours. TMABr (0.149 g, 0.097 mmol) was added and reacted for another 24 hours. The mixtures were filtered with a 0.45 μm hydrophilic syringe filter. The solution was then placed on a hotplate at 80 °C. After 24 hours, the crystals were collected, washed with DMSO, and dried on a hotplate at 80 °C for another 24 hours.

Perovskite solution mixing

The masses of precursors used to form perovskite inks presented in this study are listed in Table 1. 10.1 mg of methylammonium chloride (MACl), 425 μL of 2-methoxyethanol (2ME), and 50 μL of L-α-phosphatidylcholine solution (2 mg mL^{-1} in 2ME) were added to all compositions. The solutions were shaken with a mechanical shaker for >3 hours. Then 25 μL of NMP was added shortly before use, and all the inks were subsequently filtered through a 0.2 μm PTFE syringe filter.

Solar cell fabrication

Patterned 3.25 × 7.5 cm glass/ITO substrates (X07-15A-2308) were wiped using isopropanol and a textile wipe. The cleaned substrates were then ozone treated for 1 hour before depositing the SnO_2 layer. The SnO_2 layer was prepared by chemical bath deposition (CBD) for modules, and blade coating nanoparticles for pixel devices. For CBD, we followed a previous report,[52] except we used ITO instead of fluorine doped tin oxide (FTO) and dipped it in a water bath at 75 °C for 6 h. For blade-coated SnO_2, a solution containing SnO_2 nanoparticles in de-ionized water (1 : 6, volume ratio) was deposited on the ITO glass using a blade coater (ZAA 2300 Proceq-Automatic film applicator, Screening Eagle) at a speed of 10 mm s^{-1}, with gap height of 150 μm on a 71 °C hot plate. The substrates were then annealed at 150 °C for 30 min, followed by ozone treatment for 15 minutes. 3 mg per mL KCl solution in de-ionized water was spin coated at 3500 rpm for 20 s, followed by annealing at 150 °C for 15 minutes. The perovskite inks were blade coated at a speed of 10 mm s^{-1}, with gap height of 200 μm at ambient temperature (∼20 °C). During blade coating, N_2 (25 psi) was blown directly on the wet perovskite film. The perovskite film was then annealed at 130 °C until it turned black, and then at 150 °C for 20 min. OAI (4 mg mL^{-1} in IPA) was blade coated at 30 mm s^{-1}, with a gap height of 75 μm, using a base heat of 60 °C, and subsequently annealed at 100 °C for 10 minutes. 100 mg Spiro-OMeTAD was dissolved in 1.1 mL CB, then 23 μL Li-TFSI (520 mg mL^{-1} in ACN), 39 μL *t*BP, and 10 μL Co(III) TFSI (375 mg mL^{-1} in ACN) were added. The Spiro-OMeTAD layer was blade coated at 49 °C and at a speed of 30 mm s^{-1}, with a gap height of 150 μm. Finally, 80 nm gold was deposited by an Angstrom Engineering Inc. thermal evaporator under a vacuum of 10^{-6} torr. All the layers except for gold were deposited in ambient air with varying humidity conditions. Reported champions and statistics for both indoor light and 1 sun correspond to different batches fabricated under similar ambient conditions. The films for the $FAPbI_3$; FAPI/CPB; +CsI comparative study under indoor light were fabricated under 45 ÷ 58% RH, the ones for the FAPI/CPB; +CsI, $PbBr_2$; +$PbBr_2$ and $PbBr_2$ optimization, under 40 ÷ 50% RH, and 1 sun champions were fabricated under 20 ÷ 35% RH.

Solar module fabrication

P1 scribing was performed by Shang Yang Solar using a pulsed laser with a 1064 nm wavelength, 50 nanosecond pulse duration, speed of 300 mm s^{-1}, power of 6.7 W, 50 kHz frequency and a cut width of 50 μm. For P2 scribing, a Trotec Speedy 360 CO_2 laser emitting a 10 μm wavelength beam was utilized. The scribing parameters for P2 included a speed of 17.75 cm s^{-1}, power of 7.8 W, pulse per inch (PPI) of 1000, and a width of 200 μm. Finally, P3 involved depositing a 80 nm thick gold electrode with a width of 1 mm using a deposition mask in an EvoVac thermal evaporation system by Angstrom Engineering Inc. under a vacuum of 10^{-6} torr.

Characterization

X-ray diffraction (XRD) measurements were done with a PANalytical Empyrean system using a Cu (Kα, 1.5406 Å) source. Scanning electron microscopy (SEM) images were obtained with a Hitachi S-4800 FESEM, equipped for energy-dispersive X-ray spectroscopy (EDX) as well. Photoluminescence (PL) spectroscopy was carried out by UV-Vis AVENTES spectrometer (AvaSpec-ULS2048CL-EVO-RS) in the reflection mode ranging from 700 to 900 nm in a dark room. Absorption spectra were measured using an ultraviolet/visible spectrometer (Lambda 1050, PerkinElmer). TRPL measurements were performed on an Edinburgh Instruments OB920 Single Photon Counting system. The samples were excited using a 510 nm pulsed laser diode. External quantum efficiency (EQE) measurements were performed with a PTS-1-SR (Sciencetech Inc.). 1 sun photovoltaic parameters were measured with a Newport Oriel sol-3A (class AAA) solar simulator at standard 1.5 AM. solar irradiance, calibrated using a reference silicon solar module. Measurements under non-standardized indoor-light photovoltaic parameters were measured with a custom-designed white LED light. Its irradiance was measured by a Thorlabs Inc. S401C Thermal Power Sensor. Calibrated indoor-light photovoltaic parameters were measured with a custom-designed white LED light calibrated using an SRI 6014b Silicon Calibrated Reference Photovoltaic Cell with a Filtered Glass Window from the National Institute of Standards and Technology (NIST) calibrated under the IEC TS 62607-7-2:2023 standard for a B4 LED source with a 3.1321 W m^{-2} irradiance. The photovoltaic parameters for pixels were acquired using masks defining the illuminated areas. All *JV* curves were recorded with an Ossila source meter by scanning the cell from 1.20 V (1.10 V for indoor light, and 7 V for modules) to −0.05 V (backward) or from −0.05 V to 1.20 V (1.10 V for indoor light, and 7 V for modules) (forward), with scanning speeds of 45 mV s^{-1} for indoor light and 90 mV s^{-1} for 1 sun analysis. For operational stability measurements, encapsulated perovskite solar cells were placed in a custom-designed white LED light, and data was recorded with an Ossila source meter with time interval of 1 h between each measurement. All *JV* data was acquired in ambient-air conditions. If the J_{SC} of a pixel exceeded the value obtained from EQE (Fig. S11†), we reduced it by a factor determined from the ratio of the integrated J_{SC} in Fig. S11† to its J_{SC} measured by the IV source. The non-standardized indoor light *JV* curves were smoothed for visualization only. The relative difference of the PCE averages between backward and forward scans under a calibrated white LED source were 6.1% relative PCE higher backward scan for CBD/FAPI, 7.2% relative PCE higher backward scan for +CsI, $PbBr_2$, and 10.2% relative PCE higher forward scan for +10% $PbBr_2$.

Data availability

The data supporting this article, including the code used for calculation of maximum PCE ("max_PCE_calculation.py"), the sample data used to test the code ("sample_data.csv"), the *JV* and EQE curves in a machine-readable format ("JV_curves_FIGURE_xx.xlsx", "EQE_FIGURE_S11.xlsx"), and other supporting information referenced in the "Results and discussion" section ("SI.docx") have been included as part of the ESI.†

Author contributions

Conceptualization: VMA, MIS. Methodology: VMA, WW, MRK, SD. Investigation: VMA, WW, DZ, SQ, VY, YA, AA, MA, MIS. Visualization: VMA. Funding acquisition; project administration; supervision: MIS. Writing – original draft: VMA, MIS. Writing – review & editing: VMA, YA, MIS.

Conflicts of interest

There are no conflicts to declare.

Acknowledgements

We thank Solaires Entreprises Inc. and Canada's Natural Sciences and Engineering Research Council (ALLRP 561355-20) for their financial support. M. I. S. is grateful to the NSERC (RGPIN2020-04239), the Canadian Foundation for Innovation and B. C. Knowledge Development Fund (40326), and the Canada Research Chairs Program (CRC-2019-00297) for financial support.

References

1 L. Quan, B. Rand, R. Friend, S. Mhaisalkar, T. Lee and E. Sargent, Perovskites for Next-Generation Optical Sources, *Chem. Rev.*, 2019, **119**, 7444–7477.

2 National Renewable Energy Laboratory, *Best Research-Cell Efficiency Chart*, **https://www.nrel.gov/pv/cell-efficiency.html**, accessed: March 19th, 2025.

3 F. H. Alharbi and S. Kais, Theoretical limits of photovoltaics efficiency and possible improvements by intuitive approaches learned from photosynthesis and quantum coherence, *Renewable Sustainable Energy Rev.*, 2015, **43**, 1073–1089.

4 A. Ritcher, M. Hermle and S. W. Glunz, Reassessment of the limiting efficiency for crystalline silicon solar cells, *IEEE J. Photovoltaics*, 2013, **3**, 1184–1191.

5 A. Augusto, J. Karas, P. Balaji, S. G. Bowden and R. R. King, Exploring the practical efficiency limit of silicon solar cells using thin solar-grade substrates, *J. Mater. Chem. A*, 2020, **8**, 16599–16608.

6 O. Grånäs, D. Vinichenko and E. Kaxiras, Establishing the limits of efficiency of perovskite solar cells from first principles modeling, *Sci. Rep.*, 2016, **6**, 36108.

7 A. A. B. Baloch, M. I. Hossain, N. Tabet and F. H. Alharbi, Practical Efficiency Limit of Methylammonium Lead Iodide Perovskite (CH3NH3PbI3) Solar Cells, *J. Phys. Chem. Lett.*, 2018, **9**, 426–434.

8 M. A. Green, E. D. Dunlop, M. Yoshita, N. Kopidakis, K. Bothe, G. Siefer, D. Hinken, M. Rauer, J. Hohl-Ebinger and X. Hao, Solar cell efficiency tables (Version 64), *Prog. Photovoltaics Res. Appl.*, 2024, **32**, 425–441.

9 M. Freunek, M. Freunek and L. M. Reindl, Maximum Efficiencies of Indoor Photovoltaic Devices, *IEEE J. Photovoltaics*, 2013, **3**, 59–64.

10 J. K. W. Ho, H. Yin and S. K. So, From 33% to 57% – an elevated potential of efficiency limit for indoor photovoltaics, *J. Mater. Chem. A*, 2020, **8**, 1717–1723.

11 J. H. Noh, S. H. Im, J. H. Heo, T. N. Mandal and S. I. Seok, Chemical management for colorful, efficient, and stable inorganic-organic hybrid nanostructured solar cells, *Nano Lett.*, 2013, **13**, 1764–1769.

12 J. Xu, *et al.*, Triple-halide wide-band gap perovskites with suppressed phase segregation for efficient tandems, *Science*, 2020, **367**, 1097–1104.

13 K. Xiao, Y. Lin, M. Zhang, R. Oliver, X. Wang, Z. Liu, X. Luo, J. Li, D. Lai, H. Luo, R. Lin, J. Xu, Y. Hou, H. Snaith and H. Tan, Scalable processing for realizing 21.7% -efficient all-perovskite tandem solar modules, *Science*, 2022, **376**, 762–767.

14 S. Shcherbachenko, O. Astakhov, Z. Liu, L. Kin, C. Zahren, U. Rau, T. Kirchartz and T. Merdzhanova, High-Bandgap Perovskites for Efficient Indoor Light Harvesting, *Adv. Energy Sustainability Res.*, 2024, **5**, 2400032.

15 M. Wang, Q. Wang, J. Zhao, Y. Xu, H. Wang, X. Zhou, S. Yang, Z. Ci and Z. Jin, Low-Trap-Density CsPbX3 Film for High-Efficiency Indoor Photovoltaics, *ACS Appl. Mater. Interfaces*, 2022, **14**, 11528–11537.

16 C. Kim, M. Perera, M. Katz, D. Martineau and S. Hashimi, Performance Evaluation of Carbon-Based Printed Perovskite Solar Cells under Low-Light Intensity Conditions, *Adv. Eng. Mater.*, 2022, **24**, 2200747.

17 C. Li, Y. Liang, Y. Zhang, L. Du, J. Min and Z. Li, Enhanced Efficiency and Stability of Wide-Bandgap Perovskites via Br-Rich Bulk and Surface 2D Passivation for Indoor Photovoltaics, *Sol. RRL*, 2024, **8**, 2400231.

18 C. Li, H. Sun, D. Dou, S. Gan and L. Li, Bipolar Pseudohalide Ammonium Salts Bridged Perovskite Buried Interface

toward Efficient Indoor Photovoltaics, *Adv. Energy Mater.*, 2024, 2401833.

19 C. Liu, T. Yang, W. Cai, Y. Wang, X. Chen, S. Wang, W. Huang, Y. Dua, N. Wu, Z. Wang, Y. Yang, J. Feng, T. Niu, Z. Ding and K. Zhao, Flexible Indoor Perovskite Solar Cells by In Situ Bottom-Up Crystallization Modulation and Interfacial Passivation, *Adv. Mater.*, 2024, **36**, 2311562.

20 X. He, J. Chen, X. Ren, L. Zhang, Y. Liu, J. Feng, J. Fang, K. Zhao and S. Liu, 40.1% Record Low-Light Solar-Cell Efficiency by Holistic Trap-Passivation using Micrometer-Thick Perovskite Film, *Adv. Mater.*, 2021, **33**, 2100770.

21 Z. Skafi, *et al.*, Highly Efficient Flexible Perovskite Solar Cells on Polyethylene Terephthalate Films via Dual Halide and Low-Dimensional Interface Engineering for Indoor Photovoltaics, *Sol. RRL*, 2023, **7**, 2300324.

22 K. Wang, *et al.*, Ion–Dipole Interaction Enabling Highly Efficient CsPbI3 Perovskite Indoor Photovoltaics, *Adv. Mater.*, 2023, **35**, 2210106.

23 C. Teixeira, P. Spinelli, L. A. Castriotta, D. Müller, S. Öz, L. Andrade, A. Mendes, A. Di Carlo, U. Würfel, K. Wojciechowski and D. Forgács, Charge Extraction in Flexible Perovskite Solar Cell Architectures for Indoor Applications – with up to 31% Efficiency, *Adv. Funct. Mater.*, 2022, **32**, 2206761.

24 J. Xu, S. K. Podapangi, S. H. Reddy, L. A. Castriotta, A. Di Carlo and T. M. Brown, Key Parameters and Thresholds Values for Obtaining High Performance Perovskite Solar Cells Indoors from Full Br Compositional and Bandgap Engineering, *ACS Appl. Energy Mater.*, 2023, **6**, 10215–10224.

25 B. Hamadani, G. Neupane, S. Fu, Z. Song and Y. Yan, Insights into the Open Circuit Voltage of Perovskite Solar Cells under Low Indoor Lighting, *J. Phys. Chem. C*, 2024, **128**, 6198–6205.

26 Z.-E. Shi, T.-H. Cheng, C.-H. Lung, C.-W. Lin, C.-L. Wang, B.-H. Jiang, Y.-S. Hsiao and C.-P. Chen, Achieving over 42% indoor efficiency in wide-bandgap perovskite solar cells through optimized interfacial passivation and carrier transport, *J. Chem. Eng.*, 2024, **498**, 155512.

27 B. Hamadani and M. Campanelli, Photovoltaic Characterization under Artificial Low Irradiance Conditions Using Reference Solar Cells, *IEEE J. Photovoltaics*, 2020, **10**, 1119–1125.

28 Y. Cui, L. Hong, T. Zhang, H. Meng, H. Yan, F. Gao and J. Hou, Accurate photovoltaic measurement of organic cells for indoor applications, *Joule*, 2021, **5**, 1011–1023.

29 A. Venkateswararao, J. K. W. Ho, S. K. So, S. Liu and K. Wong, Device characteristics and material developments of indoor photovoltaic devices, *Mater. Sci. Eng., R*, 2020, **139**, 100517.

30 National Institute of Standards & Technology, *Standard Reference Instrument Series 6014: Calibrated Reference Photovoltaic Cell*, 2024, retrieved from **https://www.nist.gov/sri/sri-terms-and-conditions**.

31 X. Tan, S. Wang, Q. Zhang, H. Liu, W. Li, L. Zhu and H. Chen, Stabilizing CsPbI3 perovskite for photovoltaic applications, *Matter*, 2023, **6**, 691–727.

32 E. T. Hoke, D. J. Slotcavage, E. R. Dohner, A. R. Bowring, H. I. Karunadasa and M. D. McGehee, Reversible photo-induced trap formation in mixed-halide hybrid perovskites for photovoltaics, *Chem. Sci.*, 2015, **6**, 613–617.

33 A. J. Barker, A. Sadhanala, F. Deschler, M. Gandini, S. P. Senanayak, P. M. Pearce, E. Mosconi, A. J. Pearson, Y. Wu, A. R. S. Kandada, T. Leijtens, F. De Angelis, S. E. Dutton, A. Petrozza and R. H. Friend, Defect-Assisted Photoinduced Halide Segregation in Mixed-Halide Perovskite Thin Films, *ACS Energy Lett.*, 2017, **2**, 1416–1424.

34 C. M. Sutter-Fella, Q. P. Ngo, N. Cefarin, K. L. Gardner, N. Tamura, C. V. Stan, W. S. Drisdell, A. Javey, F. M. Toma and I. D. Sharp, Cation-Dependent Light-Induced Halide Demixing in Hybrid Organic-Inorganic Perovskites, *Nano Lett.*, 2018, **18**, 3473–3480.

35 R. Cheng, C. Chung, H. Zhang, F. Liu, W. Wang, Z. Zhou, S. Wang, A. B. Djurišić and S. Feng, Tailoring Triple-Anion Perovskite Material for Indoor Light Harvesting with Restrained Halide Segregation and Record High Efficiency Beyond 36%, *Adv. Energy Mater.*, 2019, **9**, 1901980.

36 B. Conings, J. Drijkoningen, N. Gauquelin, A. Babayigit, J. D'Haen, L. D'Olieslaeger, A. Ethirajan, J. Verbeeck, J. Manca, E. Mosconi, F. De Angelis and H. Boyen, Intrinsic Thermal Instability of Methylammonium Lead Trihalide Perovskite, *Adv. Energy Mater.*, 2015, **5**, 1500477.

37 E. J. Juarez-Perez, L. K. Ono, M. Maeda, Y. Jiang, Z. Hawash and Y. Qi, Photodecomposition and thermal decomposition in methylammonium halide lead perovskites and inferred design principles to increase photovoltaic device stability, *J. Mater. Chem. A*, 2018, **6**, 9604–9612.

38 S. Li, Y. Jiang, J. Xu, *et al.*, High-efficiency and thermally stable FACsPbI3 perovskite photovoltaics, *Nature*, 2024, **635**, 82–88.

39 D. Zhang, S. Khasnabis, W. Wang, V. Yeddu, S. Moradi, M. Awais, H.-D. Nguyen, S. B. Reinecke, Y. Haruta, R. Godin, F. Tan and M. I. Saidaminov, Cadmium-Doping Slows Trap Emptying in Ambient-Air Blade-Coated Formamidinium Lead Iodide Perovskite Solar Cells, *Adv. Energy Mater.*, 2024, **14**, 2303858.

40 Y. Peng, T. N. Huq, J. Mei, L. Portilla, R. A. Jagt, L. G. Occhipinti, J. L. MacManus-Driscoll, R. L. Z. Hoye and V. Pecunia, Lead-Free Perovskite-Inspired Absorbers for Indoor Photovoltaics, *Adv. Energy Mater.*, 2021, **11**, 2002761.

41 J. Correa-Baena, M. Saliba, T. Buonassisi, M. Grätzel, A. Abate, W. Tress and A. Hagfeldt, Promises and challenges of perovskite solar cells, *Science*, 2017, **358**, 739–744.

42 M.-J. Wu, C.-C. Kuo, L.-S. Jhuang, P.-H. Chen, Y.-F. Lai and F.-C. Chen, Bandgap Engineering Enhances the Performance of Mixed-Cation Perovskite Materials for Indoor Photovoltaic Applications, *Adv. Energy Mater.*, 2019, **9**, 1901863.

43 X. Chen, F. Yang, L. Yuan, S. Huang, H. Gu, X. Wu, Y. Shen, Y. Chen, N. Li, H.-J. Egelhaaf, C. J. Brabec, R. Zhang, F. Gao, Y. Li and Y. Li, Perfluoroalkylsulfonyl ammonium for humidity-resistant printing high-performance phase-pure

FAPbI3 perovskite solar cells and modules, *Joule*, 2024, **8**, 1–18.

44 J.-W. Lee, D.-H. Kim, H.-S. Kim, S.-W. Seo, S. M. Cho and N.-G. Park, Formamidinium and Cesium Hybridization for Photo- and Moisture-Stable Perovskite Solar Cell, *Adv. Energy Mater.*, 2015, **5**, 1501310.

45 T. Ye, S.-L. Lim, X. Li, M. Petrović, X. Wang, C. Jiang, W.-P. Goh, C. Vijila and S. Ramakrishna, Pinhole-free mixed perovskite film for bending durable mixed perovskite solar cells, *Sol. Energy Mater. Sol. Cells*, 2018, **175**, 111–117.

46 M. I. Saidaminov, A. L. Abdelhady, G. Maculan and O. M. Bakr, Retrograde solubility of formamidinium and methylammonium lead halide perovskites enabling rapid single crystal growth, *Chem. Commun.*, 2015, **51**, 17658–17661.

47 A. Redinger, S. Levcenko, C. J. Hages, D. Greiner, C. A. Kaufmann and T. Unold, Time resolved photoluminescence on Cu(In, Ga)Se2 absorbers: Distinguishing degradation and trap states, *Appl. Phys. Lett.*, 2017, **110**, 122104.

48 International Electrotechnical Commission, *IEC TS 62607-7-2:2023 Nanomanufacturing – Key Control Characteristics – Part 7-2: Nano-Enabled Photovoltaics – Device Evaluation Method for Indoor Light*, 2023.

49 W. Shockley and H. Queisser, Detailed balance limit of efficiency of p–n junction solar cells, *J. Appl. Phys.*, 1961, **32**, 510–519.

50 L. Pan, Z. Liu, C. Welton, V. V. Klepov, J. A. Peters, M. C. De Siena, A. Benadia, I. Pandey, A. Miceli, D. Y. Chung, G. N. M. Reddy, B. W. Wessels and M. G. Kanatzidis, Ultrahigh-Flux X-ray Detection by a Solution-Grown Perovskite CsPbBr3 Single-Crystal Semiconductor Detector, *Adv. Mater.*, 2023, **35**, 221840.

51 Y. Ren, Y. Haruta, S. Dayneko, J. Tao, D. Zhang, V. Yeddu, M. Bazalova-Carter and M. I. Saidaminov, Surface Chemistry of Solution-Grown CsPbBr3 Single Crystals and Their Selective Cleaning for Linear-Responsive X-ray Detectors, *ACS Mater. Lett.*, 2024, **6**, 3763.

52 J. Park, *et al.*, Controlled growth of perovskite layers with volatile alkylammonium chlorides, *Nature*, 2023, **616**, 724–730.